J. Fluid Mech. (2004), *vol.* 513, *pp.* 247–264.
DOI: 10.1017/S0022112004009942 Printed in the United Kingdom

Drag force on a sphere moving towards a corrugated wall

By N. LECOQ[1], R. ANTHORE[1], B. CICHOCKI[2], P. SZYMCZAK[2] AND F. FEUILLEBOIS[3]†

[1]CNRS UMR 6634, Université de Rouen, 76801 Saint-Étienne du Rouvray, France

[2]Institute of Theoretical Physics, Warsaw University, Hoza69, 00-681 Warsaw, Poland

[3]PMMH, CNRS UMR 7636, ESPCI, 10, rue Vauquelin, 75231 Paris Cedex 05, France

(Received 7 May 2003 and revised form 31 March 2004)

From the solution of the creeping-flow equations, the drag force on a sphere becomes infinite when the gap between the sphere and a smooth wall vanishes at constant velocity, so that if the sphere is displaced towards the wall with a constant applied force, contact theoretically may not occur. Physically, the drag is finite for various reasons, one being the particle and wall roughness. Then, for vanishing gap, even though some layers of fluid molecules may be left between the particle and wall roughness peaks, conventionally it may be said that contact occurs. In this paper, we consider the example of a smooth sphere moving towards a rough wall. The roughness considered here consists of parallel periodic wedges, the wavelength of which is small compared with the sphere radius. This problem is considered both experimentally and theoretically. The motion of a millimetre size bead settling towards a corrugated horizontal wall in a viscous oil is measured with laser interferometry giving an accuracy on the displacement of 0.1 μm. Several wedge-shaped walls were used, with various wavelengths and wedge angles.

From the results, it is observed that the velocity of the sphere is, except for small gaps, similar to that towards a smooth plane that is shifted down from the top of corrugations. Indeed, earlier theories for a shear flow along a corrugated wall found such an equivalent smooth plane. These theories are revisited here. The creeping flow is calculated as a series in the slope of the roughness grooves. The cases of a flow along and across the grooves are considered separately. The shift is larger in the former case. Slightly flattened tops of the wedges used in experiments are also considered in the calculations. It is then demonstrated that the effective shift for the sphere motion is the average of the shifts for shear flows in the two perpendicular directions. A good agreement is found between theory and experiment.

1. Introduction

Hydrodynamic interactions between particles and walls are relevant for the open problem of specifying boundary conditions for suspension flows. The Reynolds number around a small particle close to a wall is usually low and creeping-flow equations apply. For a suspension in water or air, the assumption of a low Reynolds number is true for particles typically of the order of 100 μm or less.

† Author to whom correspondence should be addressed: feuillebois@pmmh.espci.fr

However, the application of creeping-flow equations may lead to paradoxes. Classical solutions of these equations for a spherical particle close to a smooth wall by Brenner (1961), Maude (1961), Dean & O'Neill (1963), O'Neill (1964) and O'Neill & Stewartson (1967) show that the drag coefficient becomes infinite when the gap between the sphere and the wall vanishes. For instance, a sphere with radius a settling with velocity U towards a smooth horizontal plane is subjected to a lubrication drag force

$$F \simeq -\frac{6\pi a\mu}{\xi}U \tag{1.1}$$

when the non-dimensional gap ξ, that is the gap normalized by the sphere radius, becomes small compared with unity. Here μ denotes the fluid viscosity. A consequence of this lubrication effect is that the settling sphere would theoretically never touch the wall in a finite time. As recognized by Goldman, Cox & Brenner (1967*a*, *b*), the practical observation that the sphere indeed touches the wall in a finite time is the consequence of other physical phenomena, such as short-range attractive forces, like van der Waals forces. An earlier contact may also be due to surface roughness of the wall or particle. For even though a lubrication force on the scale of a bump prevents surfaces from approaching each other (using (1.1) in which a is replaced by the radius of the bump, see Smart & Leighton (1989)), the gap between the bump and the nearby surface would then become of the order of the fluid molecular dimension. Therefore, even in the presence of some remaining layers of fluid molecules, it may conventionally be said that contact occurs. This physical importance of roughness provides a strong motivation for studying the hydrodynamics of suspensions with rough surfaces. The importance of surface roughness has been also recognized for some time in the lubrication literature (see e.g. Szeri 1998 and references therein). Various theoretical approaches are based on the Reynolds equation and include the influence of surface roughness by averaging this equation. However, when the lubrication approximation is no longer valid, the Stokes equations have to be applied in the presence of a rough wall and these 'Stokes roughness' problems have received little attention.

This article is concerned with the interactions of non-touching rough surfaces, in cases when the Stokes equations have to be applied. More specifically, we will study in detail the test case of a sphere approaching a rough wall. Smart & Leighton (1989) measured the hydrodynamic effect of the surface roughness of a sphere moving perpendicularly to a smooth wall. Some of their spheres were made rough by gluing very small spheres on their surfaces. Here we do the reverse, that is we prepare walls with a definite roughness and the sphere roughness is small in comparison. The roughness considered in this article consists of periodic parallel wedges, the wavelength of which, λ, is small compared with the sphere radius (see figure 1).

The experimental technique that we use to observe the motion of a settling sphere is laser interferometry. It provides an accuracy for the sphere displacement of 0.1 μm, a significant improvement over other experiments using video. This technique was developed for this particular application, but has also been applied to other creeping-flow hydrodynamics problems (see Lecoq *et al.* 1993, 1995; Masmoudi *et al.* 1998, 2002; details on the experimental setup may be found therein).

The experimental results will show that, for a sphere in motion at a distance from the wall that is large compared with the roughness, the rough wall is equivalent to a smooth wall that is shifted down from the top of the rugosities.

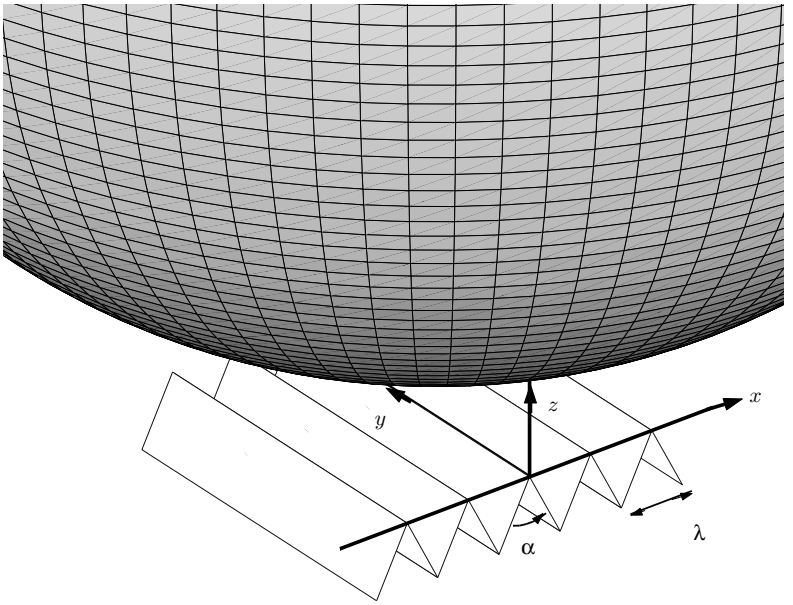

FIGURE 1. The sphere approaching the wedge-shaped wall.

In order to model these experimental results, first recall that a shear flow close to a rough wall is equivalent to a flow close to an effective smooth wall. The extensive literature on this problem will be quoted below. Consider a rough wall (like that in figure 1) with $z=0$ representing the plane at the top of the rugosities and consider e.g. a shear flow along x with velocity gradient κ far from the wall. There are two equivalent ways to consider such a flow field:

(i) either the flow velocity is written as

$$v_x = \kappa(z+b) \tag{1.2}$$

where b is the shift; that is, there is an equivalent no-slip wall at $z=-b$;

(ii) or the boundary condition on the plane $z=0$ is written as a slip condition:

$$v_x|_{z=0} = b \left.\frac{\partial v_x}{\partial z}\right|_{z=0} \tag{1.3}$$

and b is then called a 'slip length'.

For a rough wall made of parallel wedges, it is expected that the shifts (or the slip lengths) will be different for shear flows along the wedges and across them. Both problems will be considered here for the more general case of periodic corrugations. The reason for considering a general corrugated profile rather than simple wedges is that we want to take into account the deviations from the wedge geometry due to machining of the profiles used in the experiment. These deviations have non-negligible hydrodynamic consequences, as we will see.

We will then use the assumption that the flow on a scale that is large compared with the roughness, yet smaller than the sphere to wall distance, is a shear flow to which these models apply. On this basis, we will derive an expression for the drag force on a sphere approaching a rough wall on which different slip lengths apply in two perpendicular directions.

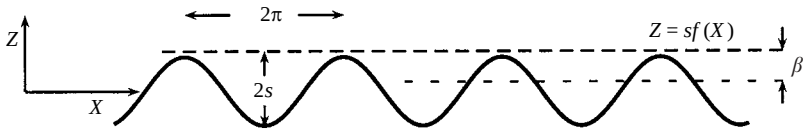

FIGURE 2. Notation for the corrugated wall.

There is a body of literature on the problem of a shear flow along a periodic rough wall. The wall profile considered here is a general periodic function with period λ along one dimension, but such that the corrugation profile is symmetric. That is, normalizing lengths by $\lambda/(2\pi)$, as shown in figure 2, and using capital letters for the dimensionless coordinates, the conditions for the profile $f(X)$ are

(i) $f(X+2\pi)=f(X)$,

(ii) $f(X+\pi)=-f(X)$.

Using Hocking's (1976) notation, let the dimensionless shift be $\beta=(2\pi/\lambda)b$ (see figure 2). There are two main problems: one for the flow parallel to the corrugations and one for the flow perpendicular to them. The first problem is a harmonic problem for the velocity along the wedges and the second requires a solution of the full creeping-flow or Stokes equations.

Both shear flow problems are well documented. Richardson (1971) calculated the particular case of a flow over a row of parallel and equidistant thick semi-infinite slabs by conformal mapping and Schwarz–Christoffel transformation. From his formula (4.4), we derive the following normalized shift for semi-infinite plates of zero thickness, that is the case of wedges when the angle α in figure 1 vanishes at constant λ: $\beta=2\log 2$.† Bechert & Bartenwerfer (1989) calculated flows over various profiles (sawtooth, trapezoidal valleys, blade riblets, namely wall attached barriers) by conformal mapping. Luchini, Manzo & Pozzi (1991) used the numerical boundary element technique to solve flows over sinusoidal, scalloped and sawtooth profiles. Wang (1994) calculated in particular the flow over blade riblets by a collocation technique.

For cross-flows, the Stokes equations have to be solved. Richardson (1973) calculated the cases of sinusoidal and scalloped profiles by conformal mapping. Hocking (1976) provided an interesting solution that he applied to the sinusoidal profile, improving that of Richardson (1973). However, his solution leads to numerical problems for large slopes. He then calculated the case of an infinite slope, namely of a row of semi-infinite plates of zero thickness, by the Wiener–Hopf technique, with the result: $\beta=0.5569$.‡ Luchini *et al.* (1991) applied the numerical boundary element technique to the same profiles as for the parallel flows. Davis (1993) considered in particular the case of blade riblets. He used a distribution of singularities over the

† Note that there is a misprint in the slip velocity he gives for that case (a factor 2 is missing), but the result follows easily from his equation (4.4) which is correct. There is also a misprint in Hocking's (1976) quotation of Richardson's result: a factor 4 is missing. The same result as in Richardson (1971) was obtained independently by Bechert & Bartenwerfer (1989) from the limit of a sawtooth profile and again by Jeong (2001) using the Wiener–Hopf technique. Jeong remarks that he recovers the result of Richardson (1971) but without pointing out the misprint in that paper. We have redone the calculation by conformal mapping as a check.

‡ Unaware of this paper, other authors redid this calculation independently, also with the Wiener–Hopf technique: Luchini *et al.* (1991) with the result $\beta=0.556475$; and Jeong (2001) with the result $\beta=0.5567$.

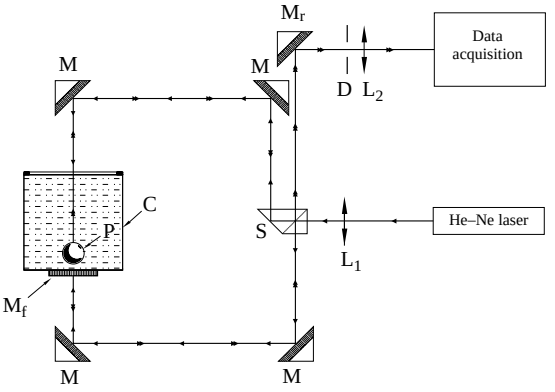

FIGURE 3. Experimental setup. C: cylindrical vessel; D: diaphragm; L_1, L_2: lenses; M: mirrors; M_f: mirror reflecting the reference beam; M_r: mirror reflecting the interference fringes; P: spherical particle; S: beam splitter.

riblets and solved a Fredholm integral equation for this distribution. Wang (1994) solved this problem independently by a collocation technique. Tuck & Kouzoubov (1995) treated the sinusoidal profile using a Hocking (1976) type of solution together with a collocation technique. Stroock *et al.* (2002) noticed that as a consequence of the anisotropy in the directions parallel and perpendicular to the grooves, the fluid particles follow helical trajectories.

We will revisit here these problems for the shear flow along and perpendicular to the corrugations. Our theoretical approach uses a solution in the spirit of Hocking (1976) and expands it as a series in the normalized half-amplitude s (see figure 2). Note that for a sinusoidal profile, s is also the maximum slope, so it will be called the 'slope' here. We will then accelerate the convergence of the series in s to extend its application range. This approach is in principle valid for any profile with limited slope.

The outline of the article is as follow. The experiment is presented in § 2. The problems of shear flows along and perpendicular to corrugations will be revisited in § 3. Then § 4 is concerned with the derivation of the drag force on a sphere approaching a periodic rough wall represented by a smooth wall with two different slip lengths. The experimental results and the model are compared and discussed in § 5. Finally, the conclusion is given in § 6.

2. Experiment

A laser interferometer was used to measure with high accuracy the vertical velocity of a spherical particle moving in a viscous fluid, using the technique described in earlier articles (see Lecoq *et al.* 1993; Masmoudi *et al.* 1998). A sketch of the experimental interferometry setup is presented in figure 3. It provides a measurement of the vertical displacement of the particle versus time. A typical example of the interferometric signal is sketched in figure 5, below. A signal variation from a maximum to a minimum (or conversely) is due to a displacement of the sphere between interference fringes of $\delta z = \Lambda/(4n)$ where $\Lambda = 632.8\,\text{nm}$ is the wavelength of the laser beam, $n = 1.404$ the index of refraction of the oil, that is $\delta z = 0.112\,\mu\text{m}$. The particle velocity is then derived after recording the displacement across several interference fringes versus time. The accuracy in the displacement is roughly equal to δz, and even a little smaller. The time is recorded with the precision of the data acquisition system, of the order of $1\,\mu\text{s}$.

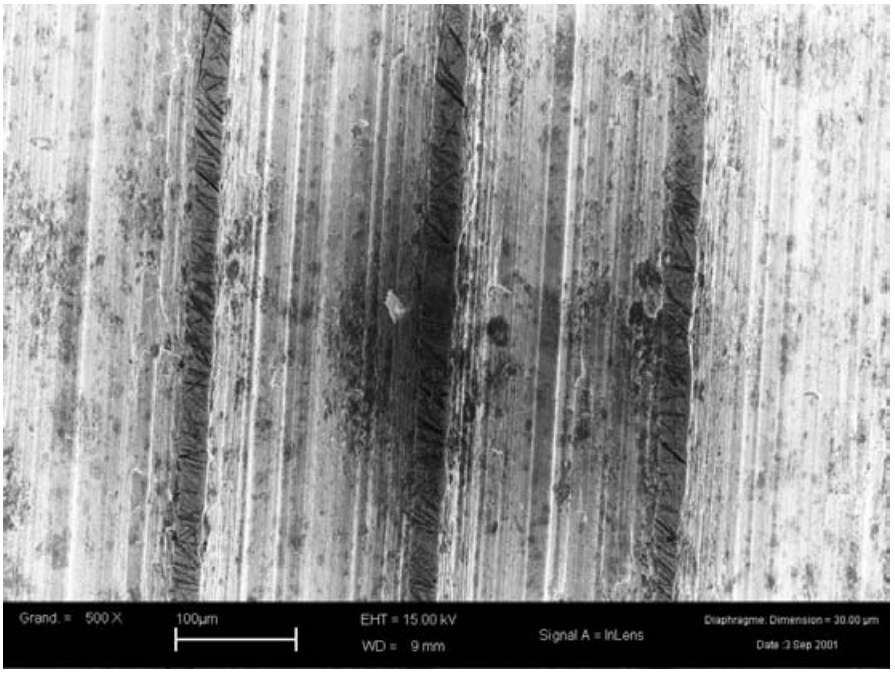

FIGURE 4. Scanning electron micrograph of a machined wall with wedges.

The settling particle is a steel ball with a mass density of about 7800 kg m^{-3} and a diameter of 6.35 mm. Departure from sphericity is negligible (lower than 0.5 μm) and the arithmetic roughness *Ra* as indicated by the manufacturer is 0.013 μm.

The sphere is embedded in a very viscous oil contained in a cylindrical vessel. This vessel (with a diameter of 50 mm and a height of 40 mm) is made of altuglas and is closed at its top by a plane glass window of optical quality.

The rough surface to be studied is placed on the inside of the lower plane endwall. Several rough surfaces were used, with periodic parallel groves with height and wavelength of the order of 100 μm. A scanning electron micrograph of one surface is shown in figure 4. It is apparent that, due to machining, the top and bottom are not sharp wedges, but are truncated as depicted schematically in figure 7 below in which they are shown as the dimensionless lengths T and B. The dimensions of all surfaces used in the experiment are given in table 1.

The vessel is filled with *Rhodorsyl 47V100000* silicone oil (manufactured by Rhône-Poulenc) of mass density 978 kg m^{-3} and kinematic viscosity 0.1 $m^2 s^{-1}$ at 25 °C. With this very large viscosity, the Reynolds number based on the sphere radius and Stokes sedimentation velocity of the particle settling in the unbounded fluid at rest is of the order of 10^{-5}. The variation of the viscosity of silicon oil with temperature is low and the oil has a Newtonian behaviour up to a shear rate of the order of 100 s^{-1}. Such a high shear rate was never attained in the experiments even when in lubrication. The oil viscosity is determined either before or after each experiment (as in Lecoq *et al.* 1993; Masmoudi *et al.* 1998) by matching the experimental result for the velocity of the sphere towards the smooth endwall (i.e. the plane glass window) with the theoretical expressions of Brenner (1961) and Maude (1961). The 'experimental' Stokes velocity obtained in this way was found to be in agreement within 0.1% with the velocity calculated from the Stokes formula using the physical data given above.

	α (deg.)	λ (μm)	$T\frac{\lambda}{2\pi}$ (μm)	$B\frac{\lambda}{2\pi}$ (μm)	$\beta_{exp}\frac{\lambda}{2\pi}$ (μm)	$\delta\beta\frac{\lambda}{2\pi}$ (μm)
$\mathscr{A}$	90	100	7	3	9 ± 1	0.3
$\mathscr{B}$	90	206	28.5	17	15.5 ± 1	1.2
$\mathscr{C}$	90	295	8	25.2	26.5 ± 2	3.2
$\mathscr{D}$	60	100	10	11.3	10.1 ± 1	0.3
$\mathscr{E}$	60	200	15	9.6	20 ± 1	1.3

TABLE 1. Data for various profiles (λ is the wavelength and the non-dimensional top T and bottom B are defined in figure 7) and experimental results β_{exp} for the shift. The uncertainty given for the experimental results corresponds to a range of four different measurements. The $\delta\beta$ uncertainty corresponds to the unknown final touching position of the sphere.

This configuration also provides an estimate of the hydrodynamic effect of the other walls. It was found in Lecoq *et al.* (1993) and Masmoudi *et al.* (2002) that the velocity of the sphere along the axis of the vessel is fitted well by the theoretical expression for the motion towards a plane wall when the sphere is within one radius of that wall. On this basis, it is expected that the motion of a sphere towards a rough wall is not affected by the other walls for similar distances.

At the beginning of the settling motion towards the rough surface, the sphere is held at the top plane window and aligned with the axis of the cylinder by using a magnet applied on the upper side of the window. Just after the sphere is released, the vessel is translated horizontally so that the laser beam reflected by the sphere is always superimposed on the incident one.

The contact position is defined, within the experimental accuracy of 112 nm in the displacement, as that at which the particle velocity vanishes for the first time. Note that the sphere may be rolling down around rugosities after this first contact and eventually come to rest in positions below the origin. A typical signal for a sphere arriving on a rough plate is displayed in figure 5 and the signal for a sphere moving towards a smooth plate is shown for comparison.

The gap d between the particle and the wall is defined from this origin and reconstructed at the end of each experiment. We then define $\xi = d/a$ as the non-dimensional distance between the sphere and the wall. When the wall is smooth, the sphere velocity normalized by its Stokes velocity decays slowly with ξ in the lubrication regime and vanishes at the 'contact' (figure 6; actually, as explained in the introduction, contact then occurs because of microrugosities). On the other hand, when the sphere approaches a rough wall, far from the contact the velocity decreases as previously and then there is a small variation in velocity and contact between the sphere and the wall occurs suddenly, that is the velocity falls to zero. In figure 6, we shifted the curve for the velocity obtained with the plane smooth wall by an amount $\Delta\xi$ so that both curves match in the far field, that is in the region where the gap $d = \xi a$ is an order of magnitude larger than the wavelength λ of corrugations. In practice, we minimized the distance between the two curves in least-squares sense, in the following matching ranges for profiles $\mathscr{A}, \mathscr{B}, \mathscr{C}, \mathscr{D}, \mathscr{E}$ described in table 1: $\xi \in [0.6, 0.8]$, $[0.7, 0.8]$, $[0.8, 1.0]$, $[0.6, 0.8]$, $[0.7, 0.8]$, respectively. Comparing the two experimental curves allows the possible influence of the other walls of the container to be taken automatically into account. But here, it happens that the ranges of matching distances are sufficiently small that the influence of the other walls of the container

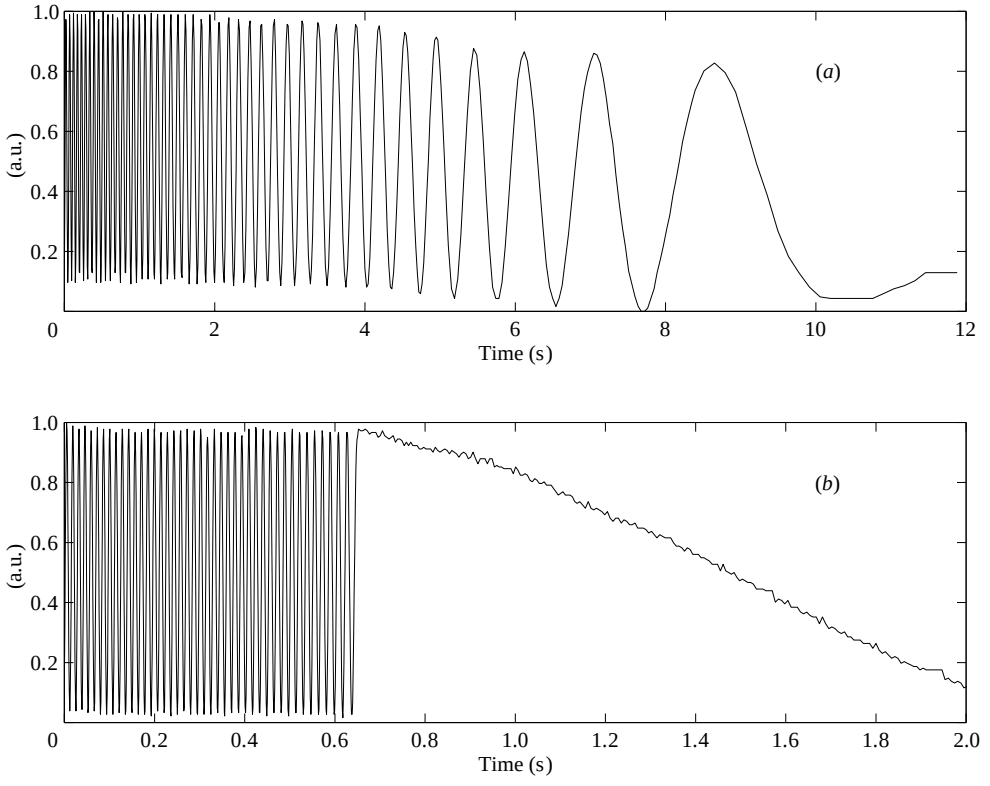

FIGURE 5. Example of recorded signals for the motion of the sphere arriving close to (*a*) a smooth and (*b*) a rough wall. The signal unit and origin of times are arbitrary. From a maximum to a minimum of the signal (or conversely), the sphere moves a distance $\delta z = \Lambda/(4n) = 0.112\,\mu\text{m}$.

is not important. Indeed, we found by comparing our experimental results for a smooth wall to the theoretical results of Brenner (1961) and Maude (1961) that the hydrodynamic interaction with the other walls becomes important only for $\xi > 3$.

If contact occurs when the sphere is touching the top of rugosities (see figure 7), then by the definition of β the dimensionless shift in figure 6 is $\Delta\xi = \beta\,\lambda/(2\pi a)$. Now, depending upon the initial position of the released sphere, it may also touch the rugosities after having penetrated a small distance into the wedges. The shift $\Delta\xi$ then is smaller than $\beta\,\lambda/(2\pi a)$ by an amount which may be estimated using some geometry to be at most

$$\delta\xi \simeq \frac{\lambda^2}{8a^2}\left(1 - \frac{T}{2\pi}\right)^2$$

where the dimensionless top length T is defined in figure 7. This variation in the shift leads to a variation in β of $\delta\beta = \delta\xi\, 2\pi a/\lambda$.

Results for the experimental dimensional shift $\beta_{exp}\,\lambda/(2\pi)$ (in μm) obtained for the various profiles are presented, together with the experimental errors, in table 1. We also include the dimensional variation $\delta\beta[\lambda/(2\pi)]$ for comparison. The error in the shift is larger for profile $\mathscr{C}$ since, because of a larger λ, we have to match in the region $\xi \in [0.8, 1.0]$ that is farther away from the wall; the sphere falls faster and the time rate of our data acquisition system then appears a little too slow, thereby decreasing the precision.

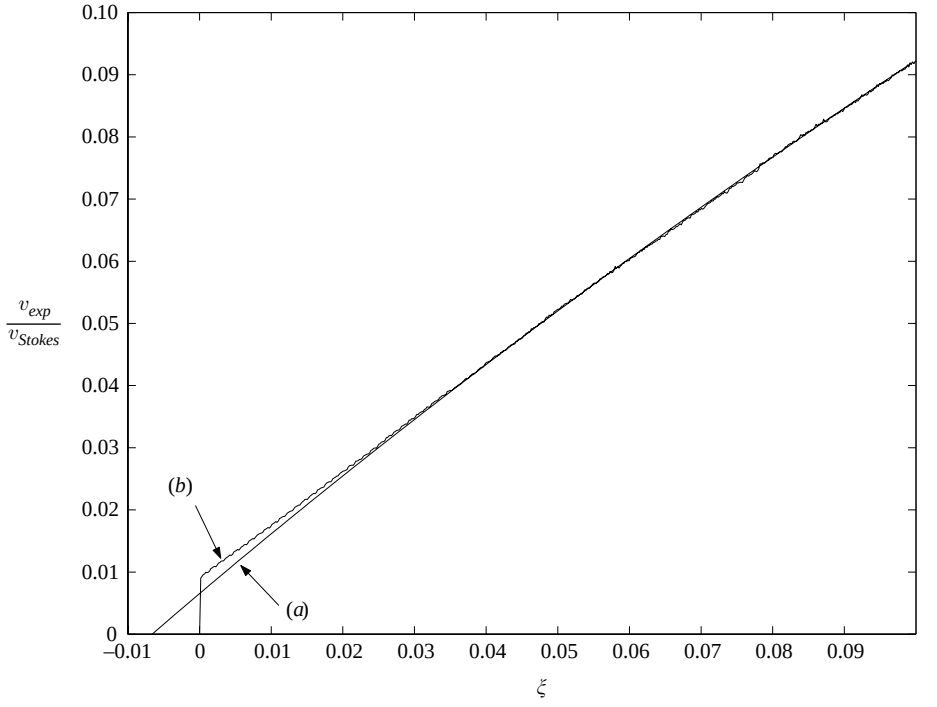

FIGURE 6. Example of normalized velocity v_{exp}/v_{Stokes} versus the non-dimensional gap ξ for a sphere arriving (a) on a smooth and (b) on a rough wall with profile $\mathscr{B}$ (see table 1) .

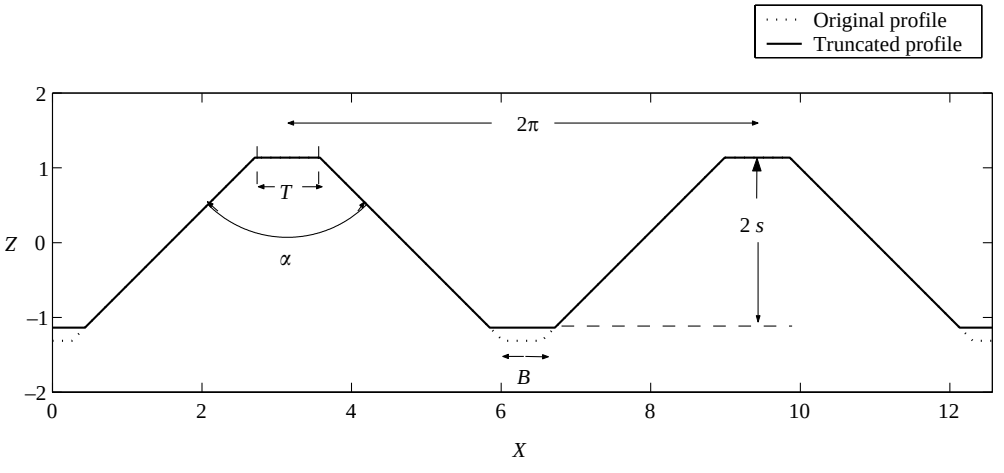

FIGURE 7. Profile $\mathscr{B}$. All lengths are made non-dimensional by using $\lambda/(2\pi)$ as a reference length. In the model, §4, the bottom length B is truncated and replaced by the larger top length T. Similar approximations are made for the other profiles.

3. Theory for the shear flow close to a periodic wall

3.1. *Description of the profiles*

A difficulty of the description is that the top and bottom part of our corrugation profiles (T and B) are different (see table 1 and figure 7). However, since a creeping

flow avoids corners in which it would dissipate energy, it is anticipated that the lower part (trough) of the profile is a dead-water region. We then use the approximation that the lower part of the profile can be truncated and the bottom length B replaced by one equal to the top length T (see figure 7), so that the profile becomes symmetric. This approximation is not strong and has the advantage of allowing a simpler description of the profile in terms of a Fourier series. Let the profile be described by $Z = sf(X)$ (figure 2), with $-1 \leqslant f(X) \leqslant 1$. As an example, a series of the form

$$f(X) = \sum_{m=0}^{M} f_{2m+1} \cos[(2m+1)X] \tag{3.1}$$

with $M = 3$ is sufficient to gives a good description of profile $\mathscr{B}$ represented in figure 7, and values calculated later use this representation (nevertheless, calculations were also done with $M = 4$ and 5 for comparison).

Let us define some characteristic quantities for the truncated profile. Let parameter p be the ratio of lengths of the flat top part T to an inclined section of the truncated profile. From figure 7,

$$p = \frac{T}{\pi - T}.$$

The dimensionless height of the truncated profile is

$$2s = (\pi - T)\cot\frac{\alpha}{2} = \frac{\pi}{1+p}\cot\frac{\alpha}{2}.$$

The numerical values of the dimensionless quantities p and s for all profiles are displayed in table 3 below.

3.2. *Series solutions for the flow fields*

We present here series solutions for the two cases of shear flows parallel and perpendicular to corrugations. The procedure for accelerating the convergence of series, § 3.3, is analogous for both cases.

Consider the case of a shear flow with rate of shear κ parallel to corrugations (see figure 1). The velocity field, normalized by $\kappa\lambda/(2\pi)$, is of the form $v(X, Z)\,\boldsymbol{e}_Y$, where $\boldsymbol{e}_Y$ denotes the unit vector along the Y-axis. This case is simpler since the Stokes equations then reduce to the Laplace equation for $v(X, Z)$ (this would more generally be true when starting from Navier–Stokes equations). A general form of solution satisfying the condition at infinity is

$$v(X, Z) = Z + d_0 + \sum_{n=1}^{\infty} d_n \mathrm{e}^{-nZ} \cos nX. \tag{3.2}$$

The equivalent smooth plane is at $Z = -d_0$ so that the normalized shift is (see figure 2):

$$\beta = s + d_0. \tag{3.3}$$

The boundary condition on the rough surface $Z = sf(X)$ is

$$0 = sf(X) + d_0 + \sum_{n=1}^{\infty} d_n \mathrm{e}^{-nsf(X)} \cos nX. \tag{3.4}$$

Note that all d_n coefficients in this equation are implicitly functions of s. By changing s to $-s$, f to $-f$ and using the condition that $f(X+\pi) = -f(X)$ we show that the d_{2m} are even in s while the d_{2m+1} are odd. Next we expand all d_n in powers of s, e.g.

d_0 takes the form

$$d_0(s) = \sum_{n=0}^{\infty} a_{0,n} s^{2(n+1)}. \tag{3.5}$$

After substituting such expansions into (3.4) as well as expanding the function

$$\mathrm{e}^{-nsf(X)} \cos nX$$

into Fourier series, we end up with a system of linear equations for the coefficients $a_{i,n}$. In particular, solving for $a_{0,n}$ allows us to find the shift from (3.3). Consider now the flow perpendicular to corrugations. The velocity field is of the form $\boldsymbol{v} = u(X, Z)\,\boldsymbol{e}_X + w(X, Z)\,\boldsymbol{e}_Z$, where $\boldsymbol{e}_X$, $\boldsymbol{e}_Z$ denote the unit vectors along the X-, Z-axes, respectively. Stokes equations give the biharmonic equation for the stream function $\psi(X, Z)$. The solution for ψ that vanishes at infinity is written, following Hocking (1976), in the form

$$\psi(X, Z) = \tfrac{1}{2}Z^2 + d_0 Z + g_0 + \sum_{n=1}^{\infty} (d_n Z + g_n)\mathrm{e}^{-nZ} \cos nX, \tag{3.6}$$

so that the velocity along X is

$$u(X, Z) = \frac{\partial \psi(X, Z)}{\partial Z} = Z + d_0 + \sum_{n=1}^{\infty} (-n d_n Z + d_n - n g_n)\mathrm{e}^{-nZ} \cos nX. \tag{3.7}$$

Like the parallel case, the equivalent smooth plane is at $Z = -d_0$, so that the normalized shift is also defined by (3.3). The no-slip boundary condition on the profile $Z = sf(X)$ is written as $\psi = 0$ and $u = 0$, giving two equations for the unknown coefficients d_n, g_n. The d_n, g_n are sought as series in s. Again here, d_0 is given by an expansion like (3.5). Substituting the series for d_n, g_n into the boundary conditions and expanding in s and in Fourier series provides linear equations for the unkown coefficients in the series. Compared with the parallel case, the number of equations is doubled, but the calculation is analogous.

3.3. *Accelerating the convergence of series*

Unfortunately, the series $\sum_{n=0}^{\infty} a_{0,n} s^{2(n+1)}$ is slowly convergent. However, as coefficients $a_{0,n}$ are of alternating signs, the convergence can be accelerated by use of the Euler transformation (see e.g. Knopp 1958)

$$a_{0,k} \to b_k = \sum_{n=0}^{k} \binom{k}{n} a_{0,n-k}. \tag{3.8}$$

In this way, we obtain

$$d_0 = \sum_{k=0}^{\infty} b_k \zeta^{k+1}, \tag{3.9}$$

where we define

$$\zeta = \frac{s^2}{1 + s^2}. \tag{3.10}$$

But the series in (3.9) is still slowly convergent as shown in table 2 for the example case of the flow perpendicular to the corrugations of profile $\mathscr{B}$ (figure 7). But from the existence of the limit $\beta(s \to \infty) = \beta_\infty$ and relation (3.3) we infer that asymptotically

k	$a_{0,k}s^{2(k+1)}$	$b_k\zeta^{k+1}$	$c_k\zeta^{k+1}$
0	-1.3420	-5.8581×10^{-1}	-5.8581×10^{-1}
1	1.2808	-8.6040×10^{-2}	9.3097×10^{-2}
2	-1.7993	-6.0625×10^{-2}	1.0751×10^{-2}
3	2.6203	-3.0198×10^{-2}	2.6410×10^{-3}
4	-3.7880	-1.5121×10^{-2}	9.0354×10^{-4}
5	5.4210	-7.5908×10^{-3}	4.8566×10^{-4}
6	-7.7109	-3.8840×10^{-3}	2.7037×10^{-4}
7	1.0940×10	-2.0307×10^{-3}	1.3659×10^{-4}
8	-1.5512×10	-1.0809×10^{-3}	6.1459×10^{-5}
9	2.1995×10	-5.8221×10^{-4}	2.4673×10^{-5}

TABLE 2. The improvement in the convergence of the series when using the terms $a_{0,k}s^{2(k+1)}$, $b_k\zeta^{k+1}$, $c_k\zeta^{k+1}$, in which $a_{0,k}$, b_k and c_k are defined by (3.5), (3.8) and (3.16) respectively and ζ is defined in (3.10). The case presented here corresponds to the flow perpendicular to profile $\mathscr{B}$ (see table 1), that is here represented as the Fourier series of (3.1) with $M=3$. For this profile, $s=1.14$ (see table 3).

$d_0 \to -s$ as $s \to \infty$. Thus, in terms of ζ,

$$\sum_{k=0}^{\infty} b_k\zeta^{k+1} \sim -\frac{1}{\sqrt{1-\zeta}}, \qquad \zeta \to 1. \tag{3.11}$$

Noting that the series $\sum_{k=0}^{\infty}\zeta^{k+1}/\sqrt{k}$ diverges for $\zeta\to1$ like

$$\int_0^{\infty}\frac{\zeta^x}{\sqrt{x}}\,\mathrm{d}x = \frac{2}{\sqrt{\log 1/\zeta}}\int_0^{\infty}\mathrm{e}^{-t^2}\,\mathrm{d}t \sim \frac{\sqrt{\pi}}{\sqrt{1-\zeta}} \tag{3.12}$$

we deduce that asymptotically the coefficient b_k should behave like

$$b_k \sim -\frac{1}{\sqrt{\pi k}}, \qquad k\to\infty. \tag{3.13}$$

This means that the asymptotic behaviour of the series under consideration is the same as that of the polylogarithm function $Li_{1/2}$ defined as (see Lewin 1981)

$$Li_{1/2}(\zeta) \equiv \sum_{k=1}^{\infty}\frac{\zeta^k}{\sqrt{k}}. \tag{3.14}$$

Once the asymptotic behaviour is known, we can make the convergence faster by subtracting the asymptotic terms, i.e.

$$d_0 = \sum_{k=0}^{\infty} c_k\zeta^{k+1} - \frac{1}{\sqrt{\pi}}Li_{1/2}(\zeta), \tag{3.15}$$

with

$$c_k = b_k + 1/\sqrt{\pi(k+1)}. \tag{3.16}$$

The above series converges fast for $s \simeq 2$. This is shown for the example of table 2, where the series formed with c_n is compared with the series formed with $a_{0,n}$ and b_n.

	p	s	ζ	β_{exp}	$\beta_{th\parallel}$	$\beta_{th\perp}$	β_{th}
$\mathscr{A}$	0.16	1.35	0.65	0.57 ± 0.04	0.72	0.40	0.56
$\mathscr{B}$	0.38	1.14	0.57	0.47 ± 0.02	0.60	0.34	0.47
$\mathscr{C}$	0.057	1.49	0.69	0.57 ± 0.07	0.81	0.46	0.64
$\mathscr{D}$	0.25	2.18	0.83	0.63 ± 0.04	0.80	0.39	0.60
$\mathscr{E}$	0.18	2.31	0.84	0.63 ± 0.04	0.86	0.41	0.63

TABLE 3. Comparison of β_{exp} (experiment) with β_{th} (theory) for various profiles.

3.4. *Results for the shift and comparison with other techniques*

The results for the normalized shift β for the profiles described in table 1 are displayed in table 3 for the cases of a flow parallel ($\beta_{th\parallel}$) and perpendicular ($\beta_{th\perp}$) to the corrugations. As expected, it is observed that $\beta_{th\parallel}$ is significantly larger than $\beta_{th\perp}$, that is the parallel flow penetrates the corrugations more easily. Indeed, for the flow perpendicular to corrugations, it is expected that a recirculation or dead water region exists in the bottom part.

The velocity of the flow parallel to the corrugations is harmonic and a solution may also be obtained using the classical complex-variable technique. We used Schwarz–Christoffel conformal mapping to transform the corrugation profile over a period to a line segment, as done by Bechert & Bartenwerfer (1989) for other profiles. Using this technique, we recover exactly the same results as with the expansion method of the preceding sections. As anticipated above, it is also found that changing the shape of the lower flat part does not alter much the final result for $\beta_{th\parallel}$.

The flow perpendicular to corrugations can in principle be obtained with a complex-variable technique, although with more difficulty. Here, as a check, we used the commercial FEMLAB finite element software to recalculate the flow velocity of a shear flow perpendicular to the profiles described in table 1. We used a box with dimension 50λ and fitted the velocity profile with a straight line in the region $[25\lambda, 50\lambda]$ in order to obtain $\beta_{th\perp}$. The results for $\beta_{th\perp}$ are practically the same as in table 3; only the last digit changes for some of the profiles. Flow fields were also plotted from the results of the finite element calculation and a typical case, namely for profile $\mathscr{A}$, is shown in figure 8 (only one half of the profile). The discontinuous line shows the position of the equivalent smooth plane; both our theoretical result and the ones obtained with FEMLAB are superimposed. In the lower part of the profile, the recirculation region appears clearly (dead-water area) as anticipated in the previous calculation in § 3.1.

4. Drag force on a sphere approaching an anisotropic slip plane

Consider a sphere moving with velocity $\boldsymbol{U}$ normally to a rough wall with periodic corrugations in one dimension. This wall is represented by an anisotropic slip plane W at $z = 0$, i.e. a plane on which two different slip lengths b_x, b_y apply in two principal perpendicular directions x and y. By assumption, these slip lengths are much smaller than the sphere radius a and the gap d between the sphere and the wall. We then introduce the small parameter $\epsilon = \mathrm{Sup}(b_x, b_y)/\mathrm{Inf}(a, d)$. In this model, the velocity along z is zero on the slip plane; like the boundary conditions in the x- and y-directions, this condition should be understood in an average sense.

Using the Lorentz reciprocal theorem, an expression for the drag force on the sphere is obtained in § 4.1, in terms of an integral on the plane. It is then shown in

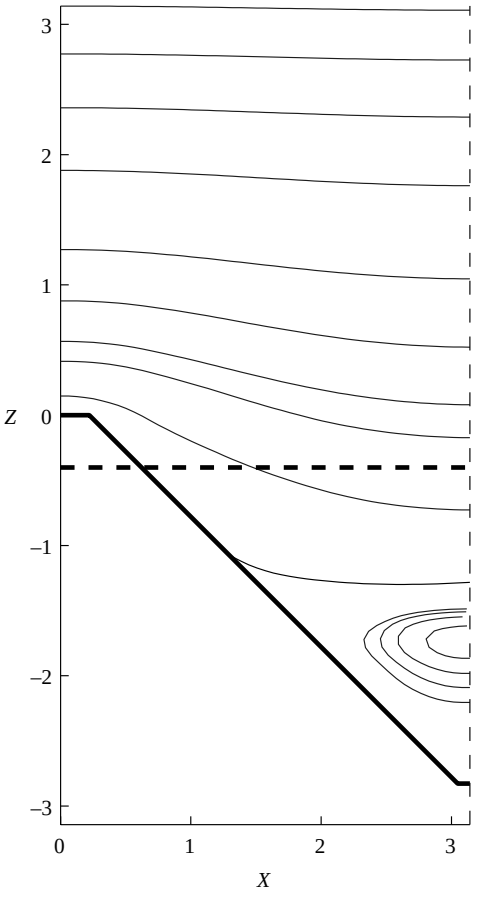

FIGURE 8. Streamlines for a shear flow perpendicular to the corrugations; example case of profile $\mathscr{A}$. The minimum value of the stream function found in the centre of the recirculation region is $\psi_{min} = -0.00624$ and displayed values of the stream function are: $\psi = -\psi_{min} \times [-0.8, -0.6, -0.4, -0.2, 0, 0.2, 2, 20, 40, 100, 200, 400, 600, 800]$. The thick dashed line shows the position of the equivalent smooth plane.

§4.2 that this expression may be written for the drag on a sphere close to an effective plane on which the no-slip condition applies; this plane is displaced from the slip plane by $(b_x + b_y)/2$.

4.1. *Expression for the drag force as an integral on the slip plane*

From the assumption of small slip lengths, the fluid velocity $\boldsymbol{v}$ for the flow around the sphere may be written as a perturbation solution $\boldsymbol{v} = \boldsymbol{v}_0 + \boldsymbol{v}_1$, where $\boldsymbol{v}_0$ is the fluid velocity for a sphere moving with velocity $\boldsymbol{U}$ normally to a no-slip plane *located at the same position* $z = 0$ *as the actual slip plane*, and $\boldsymbol{v}_1$, the perturbation due to slip, is such that $|\boldsymbol{v}_1| \ll |\boldsymbol{v}_0|$.

To summarize, the boundary conditions are the following:

(i) on the sphere S: $\boldsymbol{v} = \boldsymbol{U}$; $\boldsymbol{v}_0 = \boldsymbol{U}$;

(ii) on the plane W:

$$v_x = b_x \frac{\partial v_x}{\partial z}; \quad v_y = b_y \frac{\partial v_y}{\partial z}; \quad v_z = 0; \quad v_{0x} = v_{0y} = v_{0z} = 0.$$

Let $\boldsymbol{\sigma}_0, \boldsymbol{\sigma}_1$ be the stress tensors corresponding to $\boldsymbol{v}_0, \boldsymbol{v}_1$, respectively. Now apply the Lorentz reciprocal theorem to the flow fields $(\boldsymbol{v}_0, \boldsymbol{\sigma}_0)$ and $(\boldsymbol{v}_1, \boldsymbol{\sigma}_1)$:

$$\int_{S+W} \boldsymbol{v}_0 \cdot \boldsymbol{\sigma}_1 \cdot \boldsymbol{n} \, \mathrm{d}S = \int_{S+W} \boldsymbol{v}_1 \cdot \boldsymbol{\sigma}_0 \cdot \boldsymbol{n} \, \mathrm{d}S \tag{4.1}$$

where $\boldsymbol{n}$ is the unit vector along z. From the boundary conditions, the integral on the left-hand side reduces to $\boldsymbol{U} \cdot \boldsymbol{F}_1$, where $\boldsymbol{F}_1$ is the contribution from the flow field perturbation $(\boldsymbol{v}_1, \boldsymbol{\sigma}_1)$ to the drag on the sphere. Then, from the boundary conditions, and the form of the perturbation solution, we obtain the result that, on the plane W,

$$v_{1x} = b_x \frac{\partial v_{0x}}{\partial z} + o(\epsilon); \quad v_{1y} = b_y \frac{\partial v_{0y}}{\partial z} + o(\epsilon); \quad v_{1z} = 0$$

so that the integral on the right-hand side of (4.1) gives, to order ϵ,

$$b_x \int_W \frac{\partial v_{0x}}{\partial z} [\boldsymbol{\sigma}_0 \cdot \boldsymbol{n}]_x \, \mathrm{d}S + b_y \int_W \frac{\partial v_{0y}}{\partial z} [\boldsymbol{\sigma}_0 \cdot \boldsymbol{n}]_y \, \mathrm{d}S.$$

Since the flow field $(\boldsymbol{v}_0, \boldsymbol{\sigma}_0)$ is axisymmetric, these two integrals on W are equal and this result may be rewritten as

$$\frac{b_x + b_y}{2} \int_W \left\{ \frac{\partial v_{0x}}{\partial z} [\boldsymbol{\sigma}_0 \cdot \boldsymbol{n}]_x + \frac{\partial v_{0y}}{\partial z} [\boldsymbol{\sigma}_0 \cdot \boldsymbol{n}]_y \right\} \mathrm{d}S.$$

From the continuity condition $\nabla \cdot \boldsymbol{v}_0 = 0$ and the no-slip boundary condition for $\boldsymbol{v}_0$ on W, $\partial v_{0z}/\partial z = 0$ there, so that we can write the result from the reciprocal theorem (4.1) as

$$\boldsymbol{U} \cdot \boldsymbol{F}_1 = \frac{b_x + b_y}{2} \int_W \frac{\partial \boldsymbol{v}_0}{\partial z} \cdot \boldsymbol{\sigma}_0 \cdot \boldsymbol{n} \, \mathrm{d}S + o(\epsilon). \tag{4.2}$$

4.2. *Equivalent no-slip plane*

In this subsection, we write an expression for the drag force on a sphere centred at a distance $l + \delta l$ from a no-slip plane, in terms of the drag force when the distance is l. The simple formula obtained here complements the preceding result and allows us to find an equivalent no-slip plane.

Consider the following flow fields:

(i) $(\boldsymbol{v}_0, \boldsymbol{\sigma}_0)$ with boundary conditions
on the sphere S: $\boldsymbol{v}_0 = \boldsymbol{U}$;
on the plane $z = 0$: $\boldsymbol{v}_0 = 0$.

(ii) $(\boldsymbol{v}', \boldsymbol{\sigma}')$ with boundary conditions
on the sphere S: $\boldsymbol{v}' = \boldsymbol{U}$;
on the plane $z = -\delta l$: $\boldsymbol{v}' = 0$.

Let $\boldsymbol{F}_0(l)$ and $\boldsymbol{F}_0(l + \delta l)$ be the force on the sphere for these two flow fields, respectively.

Applying the Lorentz reciprocal theorem using the sphere S and the plane P at $z = -\delta l$ for the flow boundaries

$$\int_{S+P} \boldsymbol{v}_0 \cdot \boldsymbol{\sigma}' \cdot \boldsymbol{n} \, \mathrm{d}S = \int_{S+P} \boldsymbol{v}' \cdot \boldsymbol{\sigma}_0 \cdot \boldsymbol{n} \, \mathrm{d}S. \tag{4.3}$$

Applying the boundary conditions, we obtain

$$\boldsymbol{U} \cdot [\boldsymbol{F}_0(l + \delta l) - \boldsymbol{F}_0(l)] = -\int_P \boldsymbol{v}_0 \cdot \boldsymbol{\sigma}' \cdot \boldsymbol{n} \, \mathrm{d}S.$$

Dividing by δl and letting $\delta l \to 0$, this becomes

$$\boldsymbol{U} \cdot \frac{\mathrm{d}\boldsymbol{F}_0(l)}{\mathrm{d}l} = \int_W \frac{\partial \boldsymbol{v}_0}{\partial z} \cdot \boldsymbol{\sigma}_0 \cdot \boldsymbol{n}\, \mathrm{d}S \tag{4.4}$$

where W represents the plane $z = 0$ as in the preceding subsection.

We remark that the integral in the right-hand side is the same as in (4.2) so that the result for the drag force on a sphere approaching an anisotropic slip plane may now be written in a simpler way:

$$\begin{aligned}\boldsymbol{U} \cdot [\boldsymbol{F}_0(l) + \boldsymbol{F}_1] &= \boldsymbol{U} \cdot \left[\boldsymbol{F}_0(l) + \left(\frac{b_x + b_y}{2}\right) \frac{\mathrm{d}\boldsymbol{F}_0(l)}{\mathrm{d}l}\right] + o(\epsilon) \\ &= \boldsymbol{U} \cdot \boldsymbol{F}_0(l + (b_x + b_y)/2) + o(\epsilon).\end{aligned}$$

Thus, omitting terms of higher order in ϵ, the projection along z of the force is

$$F = F_0\left(l + \frac{b_x + b_y}{2}\right).$$

That is, the slip plane at a distance l from the sphere centre is equivalent to a no-slip plane at a distance $l + (b_x + b_y)/2$. The effective slip length is thus the average of the slip lengths in the two principal perpendicular directions. This result is applied in particular to our problem of a corrugated wall. Using the equivalence introduced in equations (1.2) and (1.3), the effective shift length for the corrugated wall is the average of the shift lengths for the motion parallel and perpendicular to the corrugations; using the normalized quantities, with a subscript *th* to denote the theoretical results:

$$\beta_{th} = \tfrac{1}{2}(\beta_{th\parallel} + \beta_{th\perp}). \tag{4.5}$$

5. Comparison of the experimental results with the model and discussion

The comparison of experimental data with the model is presented in table 3. Theoretical values of the normalized shift are those for the flow parallel to the corrugations $\beta_{th\parallel}$, perpendicular to the corrugations $\beta_{th\perp}$ and the effective shift β_{th}, equation (4.5). The error indicated for β is estimated by adding up the error from the range of measurements (from column 6 in table 1) to $\delta\beta/2$ (from column 7 in table 1).

For profiles $\mathscr{A}$, $\mathscr{B}$ and $\mathscr{E}$, theoretical results for β are quite close to the average experimental values. For profile $\mathscr{D}$, β_{th} is within the experimental error bar for β_{exp}.

For profile $\mathscr{C}$, β_{th} is at the upper bound of the experimental error bar, which is larger than for the other profiles. This may be interpreted as follows. The process for obtaining the β_{exp} involved a matching far from the wall, in the region where the precision is lower, as explained in § 2. The experimental error may then be somewhat larger than for the other profiles. Moreover, since the profile is sharp and the wavelength is large, there is a lower probability that the sphere would fall on the tip, compared with the other profiles, so that the resulting error is $\delta\beta$ rather than $\delta\beta/2$ in this case. It is also observed that for both profiles $\mathscr{C}$ and $\mathscr{D}$, the bottom flat part of the profile presented in table 1 is such that the dimensionless value of B is larger than for the other profiles. Recall that the theoretical value β_{th} was calculated using the assumption that the profile is symmetrical, thus adjusting the bottom flat part B to the upper flat part T. Then, in particular when λ is large, i.e. for profile $\mathscr{C}$, the flow in the lower part of the groove may be responsible for the slightly lower quality of the matching of the theoretical model.

The theoretical description of the sharp wedges using a Fourier series with a few cosines may also be questioned. The finite elements numerical calculation presented in § 3.4 considered sharp angles and it was pointed out that the results for β_{th} are practically the same (only the last digit may change). On the other hand the experimental profiles, as shown in the example micrograph of figure 4, do not have very sharp angles and this may be improved in future experiments.

6. Conclusion

The anisotropy of the wedge-shaped groove patterns considered in this paper gives different effective slip boundary conditions in the two perpendicular directions. The two corresponding slip lengths were calculated from solutions of the Stokes equations for creeping flow as series in terms of the slope of the grooves. From the linearity of the Stokes equations, the cases of flows along and perpendicular to the grooves were considered separately. The slip length was found to be larger in the former case. The force on a sphere approaching such a surface perpendicularly was then obtained on the basis of the preceding results and of the Lorentz reciprocity theorem, the wavelength of the pattern being assumed to be much smaller than the gap between the sphere and the surface. It was demonstrated that the surface is equivalent to an effective smooth plane that is displaced from the top of the corrugations by a slip length that is the average of the calculated slip lengths in the two perpendicular directions.

We measured the motion of a spherical particle settling towards some model surfaces made by machining various grooves. Using laser interferometry, the particle displacement was obtained with an accuracy of 0.1 μm, even for very small gaps between the particle and the wall. It was then observed that, a few particle radii away from contact, the particle motion is equivalent to that towards an effective smooth plane. The position of this smooth plane (that also represents the slip length) could then be obtained by matching the particle motion with that for a particle moving towards a plane wall. Theoretical results for the slip length were found to be in good agreement with experiment.

More precise data could be obtained with the same interferometric technique by using other types of profiles with a well-defined geometry on the microscale. A faster data acquisition system would also improve the precision in the fast part of the trajectory, when the sphere is far from the wall. This is important for the matching used to determine the slip length.

It may be remarked that the present theoretical analysis for creeping flow may be used for larger Reynolds number provided that the gap between the sphere and the wall is small enough compared with the sphere radius, so that the flow field in the gap is in the lubrication regime. Moreover, from the above assumptions, the wavelength of grooves should be small compared with the gap width. Thus, this wavelength should be very small compared with the sphere radius. The same measurement technique may also be used for this case, provided that the data acquisition system is fast enough to record a comprehensive set of interferometric data.

REFERENCES

Bechert, D. & Bartenwerfer, M. 1989 The viscous flow on surfaces with longitudinal ribs. *J. Fluid Mech.* **206**, 105–129.

Brenner, H. 1961 The slow motion of a sphere through a viscous fluid towards a plane surface. *Chem. Engng Sci.* **16**, 242–251.

Davis, A. 1993 Periodic blocking in parallel shear or channel flow at low Reynolds number. *Phys. Fluids* A **5**, 800–809.

Dean, W. R. & O'Neill, M. E. 1963 A slow rotation of viscous liquid caused by the rotation of a solid sphere. *Mathematika* **10**, 13–24.

Goldman, A. J., Cox, R. G. & Brenner, H. 1967*a* Slow viscous motion of a sphere parallel to a plane wall. I Motion through a quiescent fluid. *Chem. Engng Sci.* **22**, 637–651.

Goldman, A. J., Cox, R. G. & Brenner, H. 1967*b* Slow viscous motion of a sphere parallel to a plane wall. II Couette flow. *Chem. Engng Sci.* **22**, 653–660.

Hocking, L. 1976 A moving fluid interface on a rough surface. *J. Fluid Mech.* **76**, 801–817.

Jeong, J.-T. 2001 Slip boundary condition on an idealized porous wall. *Phys. Fluids* **13**, 1884–1890.

Knopp, K. 1958 *Infinite Sequences and Series*. Dover.

Lecoq, N., Feuillebois, F., Anthore, N., Anthore, R., Bostel, F. & Petipas, C. 1993 Precise measurement of particle-wall hydrodynamic interactions at low Reynolds number using laser interferometry. *Phys. Fluids* A **5**, 3–12.

Lecoq, N., Feuillebois, F., Anthore, R., Petipas, C. & Bostel, F. 1995 Experimental investigation of the hydrodynamic interactions between a sphere and a large spherical obstacle. *J. Phys. Paris* II **5**, 323–334.

Lewin, L. 1981 *Polylogarithms and Associated Functions*. North Holland.

Luchini, P., Manzo, F. & Pozzi, A. 1991 Resistance of a grooved surface to parallel flow and cross-flow. *J. Fluid Mech.* **228**, 87–109.

Masmoudi, K., Lecoq, N., Anthore, R., Bostel, F. & Feuillebois, F. 2002 Accurate measurement of hydrodynamic interactions between a particle and walls. *Exps Fluids* **32**, 55–65.

Masmoudi, K., Lecoq, N., Anthore, R., May, S. & Feuillebois, F. 1998 Lubricating motion of a sphere in a conical vessel. *Phys. Fluids* **10**, 1231–1233.

Maude, A. 1961 End effects in a falling-sphere viscometer. *Brit. J. Appl. Phys.* **12**, 293–295.

O'Neill, M. E. 1964 A slow motion of viscous liquid caused by a slowly moving solid sphere. *Mathematika* **11**, 67–74.

O'Neill, M. E. & Stewartson, K. 1967 On the slow motion of a sphere parallel to a nearby wall. *J. Fluid Mech.* **27**, 705–724.

Richardson, S. 1971 A model for the boundary condition of a porous material. Part 2. *J. Fluid Mech.* **49**, 327–336.

Richardson, S. 1973 On the no-slip boundary condition. *J. Fluid Mech.* **59**, 707–719.

Smart, J. & Leighton, D. 1989 Measurement of the hydrodynamic surface roughness of noncolloidal spheres. *Phys. Fluids* A **1**, 52–60.

Stroock, A., Dertinger, S., Whitesides, G. & Ajdari, A. 2002 Patterning flows using grooved surfaces. *Anal. Chem.* **74**, 5306–5312.

Szeri, A. 1998 *Fluid Film Lubrication. Theory and design*. Cambridge University Press.

Tuck, E. & Kouzoubov, A. 1995 A laminar roughness boundary condition. *J. Fluid Mech.* **300**, 59–70.

Wang, C. 1994 The Stokes drag due to the sliding of a smooth plate over a finned plate. *Phys. Fluids* **6**, 2248–2252.